

ARTICLE

Open Access

Lead-halide Cs₄PbBr₆ single crystals for high-sensitivity radiation detection

Yang Li^{1,2}, Wenyi Shao^{1,3}, Liang Chen⁴, Juan Wang¹, Jing Nie¹, Hang Zhang¹, Silong Zhang⁵, Runlong Gao⁶, Xiao Ouyang⁷, Xiaoping Ouyang^{1,2,4} and Qiang Xu¹

Abstract

Low-dimensional perovskite materials and their derivatives with excellent optical performance are promising candidates for light-emission applications. Herein, centimeter lead-halide Cs₄PbBr₆ single crystals (SCs), which have been used for radiation detection with the indirect conversion method, were synthesized by a facile solution process. The Cs₄PbBr₆ scintillator exhibits bright green emission peaking at 525 nm and a high photoluminescence quantum yield (up to 86.7%) under 375 nm laser excitation. The Cs₄PbBr₆ SCs exhibit high sensitivity to 40 keV X-rays, with a favorable linearity with the X-ray exposure dose rate, and the detection limit is as low as 64.4 nGy_{air}/s. The scintillation time-response performance of the Cs₄PbBr₆ SCs was acquired by a time-correlated single-photon counting system under alpha-particle excitation. The Cs₄PbBr₆ SCs exhibit a very fast time response ($\tau_{av} = 1.46$ ns) to alpha particles from a ²⁴¹Am radiation source. This value is comparable to that of the commercial plastic scintillator EJ-228 ($\tau_{av} = 1.31$ ns) and much faster than that of the LYSO(Ce) scintillator ($\tau_{av} = 36.17$ ns). Conceptual X-ray imaging and alpha-particle pulse height spectroscopy experiments were also performed. These results demonstrated the potential of Cs₄PbBr₆ SCs for radiation detection applications, including X-ray imaging and charged particle detection with fast scintillation decay time and high sensitivity.

Introduction

A scintillator is a radiosensitive luminescent material that can convert the energy of incident radiation (high-energy photons or particles) into ultraviolet (UV)/visible light and constitutes a critical part of the radiation detector¹. A wide range of applications have been developed for the scintillator in medical imaging, homeland security, and high-energy physics^{2–7}. Due to their excellent scintillation performance, typical bulk scintillators such as NaI:Tl and CsI:Tl are widely used in the mature commercial market and generally involve complex, rigorous, and high-temperature fabrication procedures (Kyropoulos and Czochralski methods)⁸. The disadvantage

of these methods is that during the high-temperature procedure (>1700 °C), the generated weak oxidizing atmosphere may contaminate the melt and form inclusion defects in the crystal⁸. The gadolinium oxysulfide scintillator is relatively cheap and can be easily made into a flexible material². However, the long decay time of this scintillator results in a relatively long X-ray exposure time. Plastic scintillators usually have the advantages of a fast decay time and a low production cost, but the relatively low atomic number makes it difficult to fully deposit radiant energy⁹. Herein, an ideal scintillation material with desirable properties, such as high light yield, fast decay time, appreciable emission wavelength (matching the quantum efficiency of the photomultiplier tube), and low cost, is expected.

Recently, solution-processable metal halide perovskites (MHPs) have been demonstrated to be a promising class of materials for optoelectronic applications^{10–12}. Among the MHP family, zero-dimensional (0D) perovskite-related

Correspondence: Xiaoping Ouyang (oyxp2003@aliyun.com) or Qiang Xu (xuqiangxm@nuaa.edu.cn)

¹The Department of Nuclear Science and Engineering, Nanjing University of Aeronautics and Astronautics, 211106 Nanjing, China

²Shaanxi Engineering Research Center of Controllable Neutron Source, School of Science, Xijing University, 710123 Xi'an, China

Full list of author information is available at the end of the article

© The Author(s) 2021



Open Access This article is licensed under a Creative Commons Attribution 4.0 International License, which permits use, sharing, adaptation, distribution and reproduction in any medium or format, as long as you give appropriate credit to the original author(s) and the source, provide a link to the Creative Commons license, and indicate if changes were made. The images or other third party material in this article are included in the article's Creative Commons license, unless indicated otherwise in a credit line to the material. If material is not included in the article's Creative Commons license and your intended use is not permitted by statutory regulation or exceeds the permitted use, you will need to obtain permission directly from the copyright holder. To view a copy of this license, visit <http://creativecommons.org/licenses/by/4.0/>.

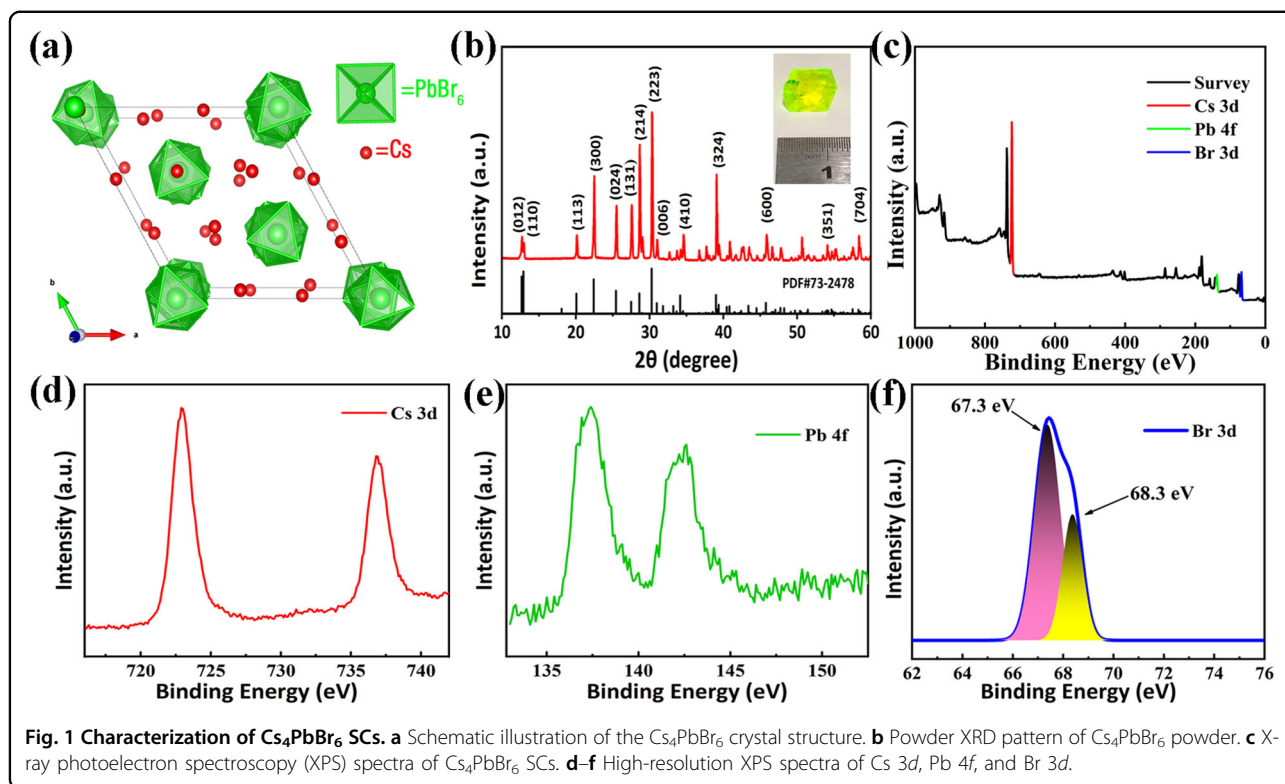


Fig. 1 Characterization of Cs_4PbBr_6 SCs. **a** Schematic illustration of the Cs_4PbBr_6 crystal structure. **b** Powder XRD pattern of Cs_4PbBr_6 powder. **c** X-ray photoelectron spectroscopy (XPS) spectra of Cs_4PbBr_6 SCs. **d–f** High-resolution XPS spectra of Cs 3d, Pb 4f, and Br 3d.

Cs_4PbBr_6 shows a completely isolated octahedron cation in the structure^{13–15}. The potential role of this structure is to localize charge carriers and provide a very strong exciton confinement, which is considered to be beneficial for light-emission performance^{16,17}. Cs_4PbBr_6 SCs have been demonstrated to have a high photoluminescence (PL) quantum yield (PLQY) at room temperature and have been used for light-emission applications^{18,19}.

Due to the high-Z atom, efficient light emission, and solution processability, Cs_4PbBr_6 -based solid powder has been developed as a scintillator for X(γ)-ray detection^{20–25}. Haibo Zeng and colleagues fabricated a large-area film based on $\text{CsPbBr}_3@/\text{Cs}_4\text{PbBr}_6$ mixed perovskite with excellent scintillation properties and achieved high contrast X-ray imaging²⁴. In our previous publication, $\text{CsPbBr}_3/\text{Cs}_4\text{PbBr}_6$ nanocrystals (NCs) exhibited desirable scintillation properties with a fast decay time (<10 ns), a fine energy resolution ($3.0 \pm 0.1\%$ at 59.6 keV) and a high light yield (64,000 photons/MeV)²⁵. However, for high-energy X(γ)-ray detection applications, these NC-based thin film scintillators cannot provide sufficient X(γ)-ray absorption. A thick, bulk single-crystal scintillator is expected for high-energy radiation applications, especially for high-energy X-ray imaging.

In this article, centimeter-sized bulk Cs_4PbBr_6 SCs were synthesized by a facile solution process. Due to its unique material structure, this 0D scintillator material exhibits a

high PLQY of up to 86.7%. A detection limit as low as $64.4 \text{ nGy}_{\text{air}}/\text{s}$ was extracted from the radiation dose-dependent X-ray radioluminescence (RL) spectra, showing the high sensitivity of Cs_4PbBr_6 SCs to 40 keV X-rays. Subsequently, scintillation time-response characteristics of Cs_4PbBr_6 SCs were obtained through a time-correlated single-photon counting (TCSPC) system under alpha-particle excitation, and conceptual X-ray imaging and alpha-particle pulse height spectrum experiments were also carried out. Our study suggests that low-cost Cs_4PbBr_6 SCs have potential in indirect radiation applications, including X-ray imaging and high-count-rate radiation detection.

Results and discussion

Cs_4PbBr_6 SCs were crystallized by a hydrobromic acid-assisted slow cooling method via reaction of CsBr with PbBr_2 ¹⁹. Figure 1a displays the unit cell of Cs_4PbBr_6 in which the $[\text{PbBr}_6]^{4-}$ anions are spatially isolated by Cs^+ cations. Centimeter-sized bulk Cs_4PbBr_6 SCs were harvested from the solution, as shown in the inset in Fig. 1b. The powder X-ray diffraction pattern demonstrates that Cs_4PbBr_6 is in the trigonal space group $R3c$ with lattice parameters $a = b = 13.83 \text{ \AA}$ and $c = 17.45 \text{ \AA}$. The position of the diffraction peaks in Fig. 1b is well aligned with previous literature^{26–28}.

XPS spectra were obtained to further investigate the elemental composition of the samples. As shown in

Fig. 1c, only Cs, Pb, and Br are observed in the crystal. The high-resolution XPS spectra of Cs 3*d*, Pb 4*f*, and Br 3*d* are shown in Fig. 1d–f. The peak positions located at 736.8 and 722.9 eV correspond to Cs 3*d* 5/2 and 3*d* 3/2, respectively. The peaks centered at 137.6 and 142.7 eV are assigned to Pb 4*f* 7/2 and 4*f* 5/2, respectively. The peak in the range 67–70 eV correlated with Br 3*d* can be well fitted with two Gaussian equations. These two peaks (68.3 and 67.3 eV) can be attributed to the Br atoms in isolated [PbBr₆]⁴⁻ of Cs₄PbBr₆ and to the Br atoms of CsBr impurities or corner-sharing [PbBr₆]⁴⁻ of CsPbBr₃, respectively, which is consistent with the previous reports²⁵.

In previous reports, the color of Cs₄PbBr₆ SCs harvested from solution during different growth stages ranged from transparent to bright green. Their PL emission band underwent an evolution from blue to green, accompanied by a sharp increase in the PLQY¹⁹. Currently, there are still many disputes about the origin of their strong bright green light^{29,30}. Several researchers attribute this phenomenon to the CsPbBr₃ nanoparticles (~2.4 eV bandgap) embedded in the Cs₄PbBr₆ matrix undergoing down-conversion emission^{28,31}. Others suggest that it should be attributed to some defect states originating from halogen (Br) vacancies^{29–31}. As shown in Fig. S1, the PL excitation spectra of Cs₄PbBr₆ SCs exhibit a bright green luminescence peak at a wavelength of 525 nm when the excitation wavelength is in the range 340–500 nm. Notably, as shown in Fig. 2a, a weak peak at ~375 nm (peak I) is observed in the temperature-dependent PL spectra, which can be attributed to two overlapping emission bands originating from different optical transitions related to Pb²⁺ ions that occupy Cs⁺ sites³². With increasing temperature, the position of peak II exhibits a blueshift, and the full-width at half-maximum increases from ~9 to 21 nm (Fig. S2). The evolution trend of peak II with temperature is consistent with our previously reported optical properties of CsPbBr₃/Cs₄PbBr₆ NCs²⁵, revealing

their consistent possibly analogical downconversion luminescence mechanism. The exciton binding energy is a key factor to be considered in measuring the luminescence performance of materials, which can be extracted by the following Arrhenius relation:²⁵

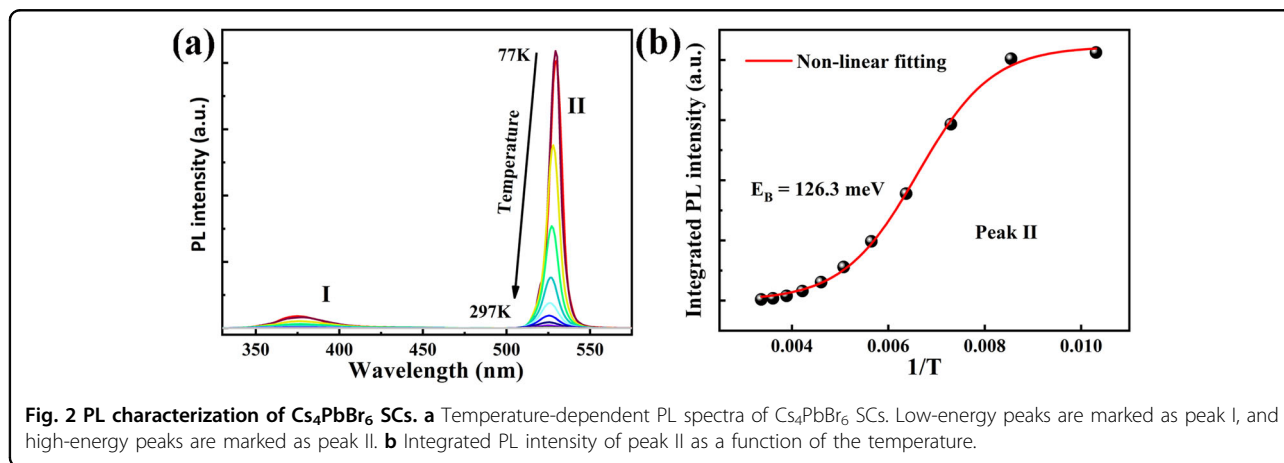
$$I_{(T)} = \frac{I_0}{1 + Ae^{-E_b/k_bT}} \quad (1)$$

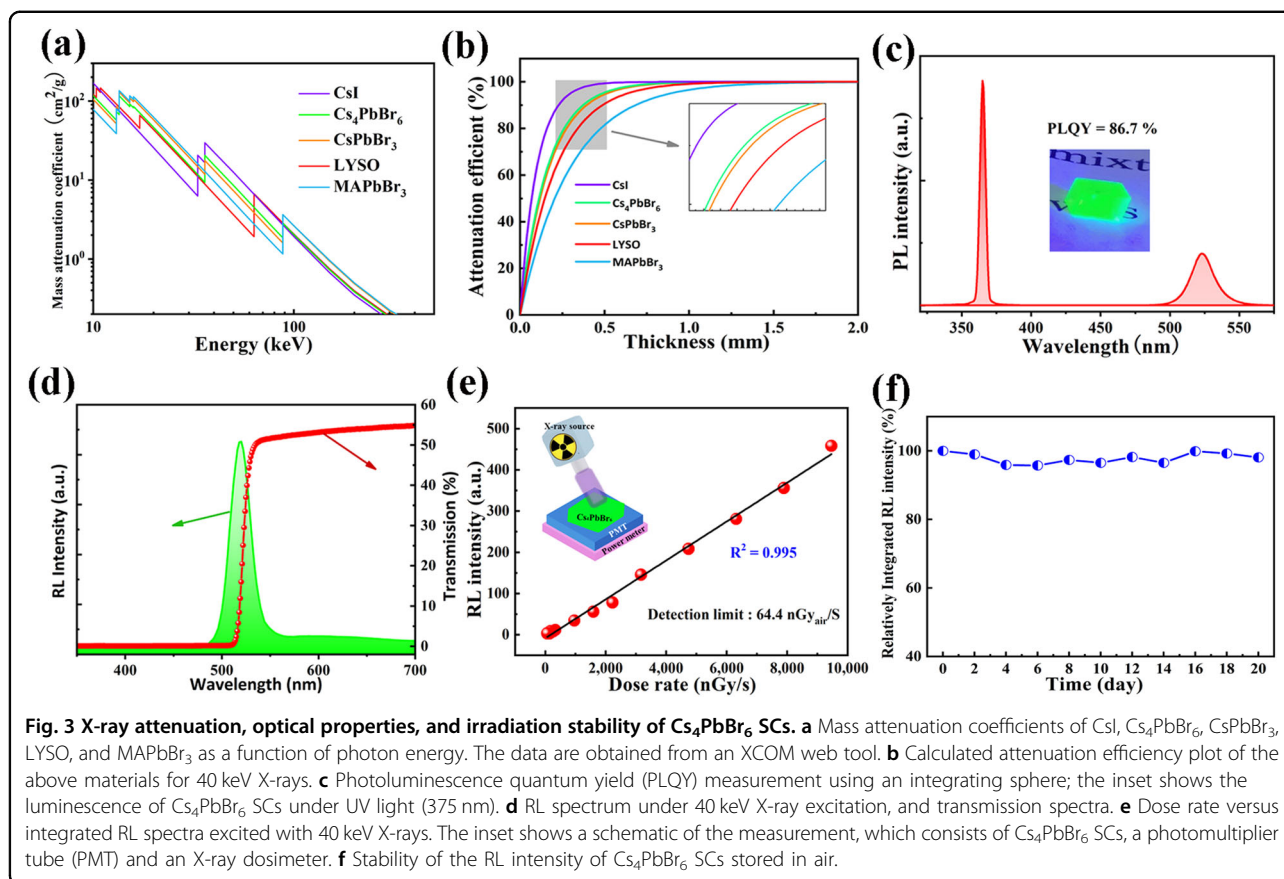
where I_0 is the integrated RL intensity at 0 K, E_b is the exciton binding energy, and k_b is the Boltzmann constant. The relationship between the integrated PL intensity of peak II and temperature can be well fitted by formula (1), as plotted in Fig. 2b. Due to the 0D crystal structure and low electronic dimensionality, the extracted binding energy of Cs₄PbBr₆ SCs is ~126.3 meV, which is larger than that of 0D (C₄H₁₄N₂)₂In₂Br₁₀ SCs or CsPbBr₃ NCs^{33,34}.

The RL of a scintillator under relatively low-energy X-rays comes from the interaction between the incident radiation and heavy atoms of the material through the photoelectric effect³⁵. In this process, a large number of electrons are generated and ejected from the lattice. The attenuation power of a material for different energy photons is related to its cross-section, which is highly dependent on the effective atomic number and density of its constituent atoms. Figure 3a shows the mass attenuation coefficients of CsI, Cs₄PbBr₆, CsPbBr₃, LYSO, and MAPbBr₃ versus the photon energy according to the XCOM database. The attenuation efficiency for 40 keV X-rays can be extracted from Fig. 3b and calculated by an exponential function:³⁶

$$\frac{I}{I_0} = e^{-\mu x} \quad (2)$$

where I_0 is the intensity of the incident photons, μ is the linear attenuation coefficient, and x is the penetration depth in the material. By comparison, although slightly lower than that of advanced CsI scintillators, the





attenuation efficiency of Cs_4PbBr_6 is higher than that of the commercial LYSO scintillator. Because of the increase in effective atomic number, the attenuation efficiency is also higher than that of the previously reported CsPbBr_3 and MAPbBr_3 perovskite scintillators^{22,37}. PLQY measurements continue to be developed to quantify the luminous efficiency of Cs_4PbBr_6 SCs (Fig. 3c). The inset in Fig. 3c shows the bright green fluorescence of Cs_4PbBr_6 SCs under ultraviolet light (375 nm)^{13,38}. The high PLQY of Cs_4PbBr_6 SCs can ensure effective radiative recombination when the photocarriers are transferred to the recombination centers during the scintillation process³⁹.

As shown in Fig. 3d, the RL spectral peak of the Cs_4PbBr_6 SCs is located at ~ 520 nm under 40 keV X-ray excitation. A single sharp absorption edge at 525 nm can also be observed from the transmission profiles (Fig. 3d). The Cs_4PbBr_6 SCs exhibit high sensitivity to 40 keV X-rays, and the response is linear over a large dose rate range (Fig. 3e). Thus, it is foreseeable that the dose rate and scintillation response should be highly correlated. The detection limit can be extracted from the fitted curve as ~ 64.4 nGy_{air}/s, which is comparable to the reported value for lead-free $\text{Cs}_2\text{Ag}_{0.6}\text{Na}_{0.4}\text{In}_{0.85}\text{Bi}_{0.15}\text{Cl}_{16}$ scintillator wafers³⁹. In addition, the integrated RL intensity of

Cs_4PbBr_6 SCs shows no apparent reduction after storage at room temperature for 20 days, which demonstrates excellent air stability (Fig. 3f).

The decay time of a scintillator represents its response rate and counting ability for incident radiation particles, which is a key factor in practical applications. To achieve high time resolution performance, a scintillator with a fast decay time is required. Therefore, a self-built TCSPC system was used to accurately obtain the scintillation time-response properties (Fig. S3)⁴⁰. Figure 4a shows the scintillation temporal profile of LYSO(Ce), Cs_4PbBr_6 , and EJ-228 excited by the alpha particles from a ²⁴¹Am radiation source at room temperature. The results of the scintillation decay time fitted by a biexponential function are tabulated in Table 1. The Cs_4PbBr_6 SCs exhibit a very fast time response ($\tau_{\text{av}} = 1.46$ ns) to alpha particles. This value is comparable to that of the commercial plastic scintillator EJ-228 ($\tau_{\text{av}} = 1.31$ ns) and much faster than that of the LYSO(Ce) scintillator ($\tau_{\text{av}} = 36.17$ ns). A comparison of the key scintillation parameters of Cs_4PbBr_6 SCs and other reported scintillator materials is shown in Table S1. The fast decay time characteristic demonstrates that the Cs_4PbBr_6 SCs can be used for applications such as fast X(γ)-ray counting.

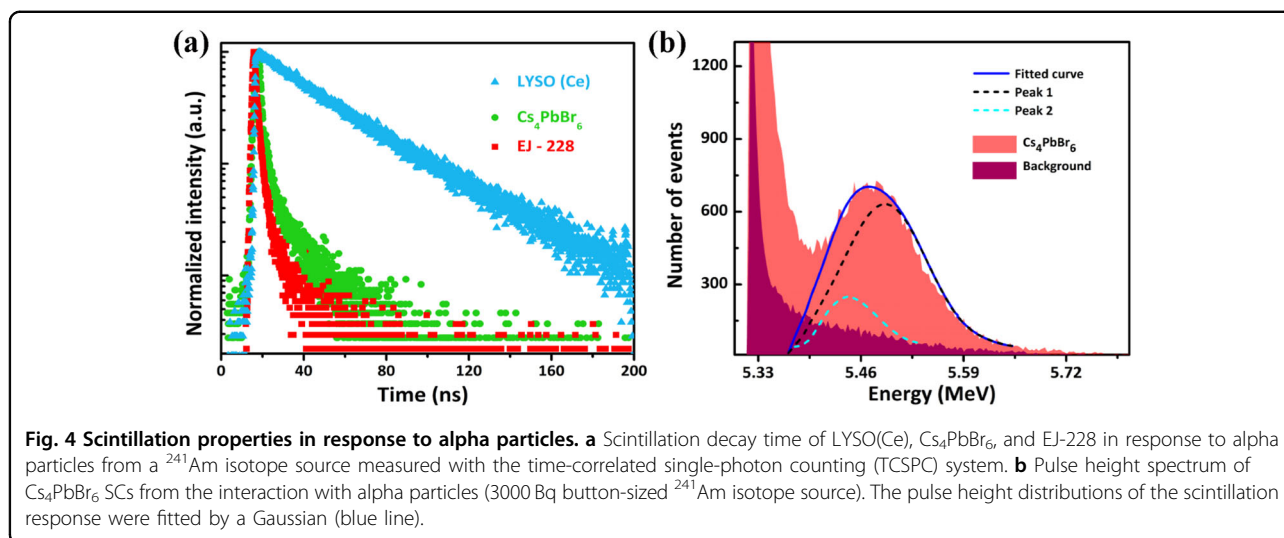


Table 1 Parameters of the fitted scintillation decay time.

Sample	A ₁ (%)	τ ₁ (ns)	A ₂ (%)	τ ₂ (ns)	τ _{av} (ns)
EJ-228	99.95	1.31	0.05	8.05	1.31
Cs ₄ PbBr ₆	99.93	1.45	0.07	12.2	1.46
LYSO(Ce)	88	30.39	12	77.69	36.17

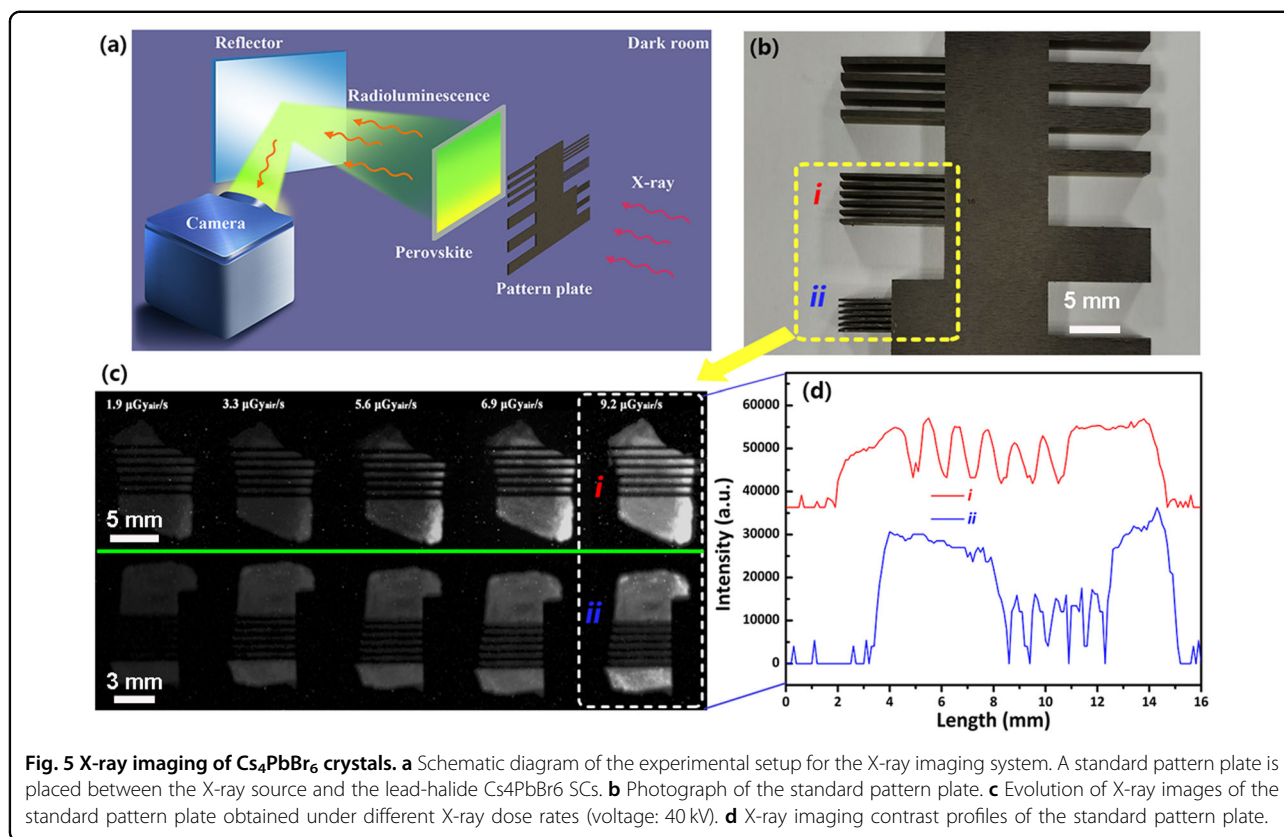
Figure 4b shows the pulse height spectrum acquired with Cs₄PbBr₆ SCs. This Gaussian-shaped peak is attributed to the two groups of alpha particles with similar energy (5.44 and 5.49 MeV) released by the ²⁴¹Am radiation source. The fitted Gaussian-shaped peak was deconvoluted into two Gaussian functions. Peak 1 (black dash-dotted) can be ascribed to the energy released by the 5.49 MeV alpha particles, and the energy resolution is estimated to be ~58.7%. Peak 2 (cyan dash-dotted) can be attributed to the 5.44 MeV alpha particles, with an energy resolution of ~51.6%. The relatively poor energy resolution of Cs₄PbBr₆ SCs may be due to the incomplete collection of scintillation photons, which is mainly affected by the photon scattering from unpolished crystals with uneven surfaces. This can be further improved by the construction of a photonic crystal structure or the polishing of the crystal surface^{41,42}

As seen from the above results, Cs₄PbBr₆ SCs feature fast time-response properties and a low detection limit, which are of great significance in reducing the radiation dose and exposure time suffered by patients in practical medical imaging applications. To perform an X-ray radiography experiment with Cs₄PbBr₆ as a scintillator, a homemade X-ray imaging system was constructed, as shown in Fig. 5a. The applied voltage and current on the X-ray tube and the measured dose rate are shown in

Table S2. Figure 5b shows a photograph of a standard pattern plate, and the interval width between the lines is 1 mm (i) and 0.6 mm (ii). The X-ray-induced RL intensity exhibits a great linear relationship with the X-ray dose rate, which has been proven in the above results. Based on this, clear X-ray images with different doses can be obtained by adjusting the current of the X-ray source (Fig. 5c). It should be noted that the dose rate of X-rays applied in this demonstrative experiment is much lower than that in practical chest computed tomography (CT)^{2,24}. The interval widths of 1 and 0.6 mm in the image can be resolved at dose rates ranging from 3.3 to 9.2 μGy_{air}/s, and the contour profile of the standard pattern plate at a dose rate of 9.2 μGy_{air}/s was extracted to provide more details (Fig. 5d). Due to the limitation of the experimental conditions, the estimated spatial resolution is at least 600 μm under a low dose rate <3.3 μGy_{air}/s. The results indicate that the Cs₄PbBr₆ SC scintillator is expected to be a promising low-dose X-ray imaging material with high sensitivity, high resolution, and fast response.

Conclusions

In conclusion, we have successfully synthesized centimeter-sized lead-halide Cs₄PbBr₆ SCs by a facile solution process. This 0D scintillator is demonstrated to have a high PLQY and a large exciton binding energy under UV light excitation. Furthermore, under X-ray exposure, it exhibits a favorable linear detection range, a low detection limit, a fast decay time, and air stability. Notably, the fast scintillation decay time of Cs₄PbBr₆ is greatly advantageous for reducing the energy accumulation in pulse amplitude spectrum experiments and decreasing the radiation exposure time in X-ray imaging applications. Future research focusing on optimization of the crystal surface quality and size of Cs₄PbBr₆ SCs is



needed to provide a material basis for possible radiation detection applications.

Acknowledgements

This work was funded by the National Natural Science Foundation of China (Grant Nos. 11705090, 11875166, and 11435010).

Author details

¹The Department of Nuclear Science and Engineering, Nanjing University of Aeronautics and Astronautics, 211106 Nanjing, China. ²Shaanxi Engineering Research Center of Controllable Neutron Source, School of Science, Xijing University, 710123 Xi'an, China. ³School of Microelectronics, Dalian University of Technology, 116024 Dalian, China. ⁴State Key Laboratory of Intense Pulsed Radiation Simulation and Effect and Radiation Detection Research Center, Northwest Institute of Nuclear Technology, 710024 Xi'an, China. ⁵School of Materials Science and Engineering, Xiangtan University, 411105 Xiangtan, China. ⁶School of Energy and Power Engineering, Xi'an Jiaotong University, 710049 Xi'an, China. ⁷Institute of Nuclear and New Energy Technology, Tsinghua University, 100084 Beijing, China

Author contributions

Q.X. and X.O. supervised the project. Y.L. and W.S. wrote the manuscript. W.S. revised the manuscript. J.W. and J.N. synthesized the lead-halide Cs_4PbBr_6 SCs. H.Z. and X.O. measured the optical properties of the lead-halide Cs_4PbBr_6 SCs. Y.L. and W.S. measured the temperature-dependent PL spectra and dose-dependent RL spectra. L.C. and Y.L. carried out the construction and experiment of the X-ray imaging system. L.C. developed the time-correlated single-photon counting system. Y.L. and L.C. conducted the pulse height spectrum measurement experiment. The manuscript was written through the contributions of all authors. All authors have approved the final version of the manuscript.

Conflict of interest

The authors declare no competing interests.

Publisher's note

Springer Nature remains neutral with regard to jurisdictional claims in published maps and institutional affiliations.

Supplementary information The online version contains supplementary material available at <https://doi.org/10.1038/s41427-021-00308-w>.

Received: 10 November 2020 Revised: 24 February 2021 Accepted: 15 March 2021.

Published online: 23 April 2021

References

- Yuan, D. Air-stable bulk halide single crystal scintillator $\text{Cs}_3\text{Cu}_2\text{I}_5$ by melt growth: intrinsic and TI-doped with high light yield. *ACS Appl. Mater. Interfaces* **12**, 38333–38340 (2020).
- Heo, J. H. et al. High-performance next-generation perovskite nanocrystal scintillator for nondestructive X-ray imaging. *Adv. Mater.* **30**, 1801743 (2018).
- Li, S., Luo, J., Liu, J. & Tang, J. Self-trapped excitons in all-inorganic halide perovskites: fundamentals, status, and potential applications. *J. Phys. Chem. Lett.* **10**, 1999–2007 (2019).
- Yang, B. et al. Lead-free halide Rb_2CuBr_3 as sensitive X-ray scintillator. *Adv. Mater.* **31**, 1904711 (2019).
- Yu, D. et al. Two-dimensional halide perovskite as β -ray scintillator for nuclear radiation monitoring. *Nat. Commun.* **11**, 3395 (2020).
- Mir, W. J. et al. Lanthanide doping in metal halide perovskite nanocrystals: spectral shifting, quantum cutting and optoelectronic applications. *NPG Asia Mater.* **12**, 9 (2020).

7. Slam, M. J. et al. Mixed-halide perovskite synthesis by chemical reaction and crystal nucleation under an optical potential. *NPG Asia Mater.* **11**, 31 (2019).
8. Lecoq, P., Gektin, A. & Korzhik, M. *Inorganic Scintillators for Detector Systems* (Springer, 2006).
9. Zhang, Y. et al. Metal halide perovskite nanosheet for X-ray high-resolution scintillation imaging screens. *ACS Nano* **13**, 2520–2525 (2019).
10. Liu, M. et al. Aluminum-doped cesium lead bromide perovskite nanocrystals with stable blue photoluminescence used for display backlight. *Adv. Sci.* **4**, 1700335–1700335 (2017).
11. Jena, A. K., Kulkarni, A. & Miyasaka, T. Halide perovskite photovoltaics: background, status, and future prospects. *Chem. Rev.* **119**, 3036–3103 (2019).
12. Quan, L. N. et al. Perovskites for next-generation optical sources. *Chem. Rev.* **119**, 7444–7477 (2019).
13. Bastiani, M. D. et al. Inside perovskites: quantum luminescence from bulk Cs_4PbBr_6 single crystals. *Chem. Mater.* **29**, 7108–7113 (2017).
14. Cha, J. et al. Photoresponse of CsPbBr_3 and Cs_4PbBr_6 perovskite single crystals. *J. Phys. Chem. Lett.* **8**, 565–570 (2017).
15. Lin, H., Zhou, C., Tian, Y., Siegrist, T. & Ma, B. Low-dimensional organometal halide perovskites. *ACS Energy Lett.* **3**, 54–62 (2018).
16. Ma, Z. et al. Pressure-induced emission of cesium lead halide perovskite nanocrystals. *Nat. Commun.* **9**, 4506–4506 (2018).
17. Saidaminov, M. I. et al. Pure Cs_4PbBr_6 : highly luminescent zero-dimensional perovskite solids. *ACS Energy Lett.* **1**, 840–845 (2016).
18. Zhang, Z. et al. Aqueous solution growth of millimeter-sized nongreen-luminescent wide bandgap Cs_4PbBr_6 bulk crystal. *Cryst. Growth Des.* **18**, 6393–6398 (2018).
19. Chen, X. et al. Centimeter-sized Cs_4PbBr_6 crystals with embedded CsPbBr_3 nanocrystals showing superior photoluminescence: nonstoichiometry induced transformation and light-emitting applications. *Adv. Funct. Mater.* **28**, 1706567.1–1706567.7 (2018).
20. Wei, H. & Huang, J. Halide lead perovskites for ionizing radiation detection. *Nat. Commun.* **10**, 1066 (2019).
21. Shao, W. et al. Gradient heterostructure perovskite single crystals enable the improvement of radiative recombination for scintillator application. *Phys. Chem. Chem. Phys.* **22**, 6970–6974 (2020).
22. Mykhaylyk, V. B., Kraus, H. & Saliba, M. Bright and fast scintillation of organolead perovskite MAPbBr_3 at low temperatures. *Mater. Horiz.* **6**, 1740–1747 (2019).
23. Wei, W. et al. Monolithic integration of hybrid perovskite single crystals with heterogeneous substrate for highly sensitive X-ray imaging. *Nat. Photonics* **11**, 315 (2017).
24. Cao, F. et al. Shining emitter in a stable host: design of halide perovskite scintillators for X-ray imaging from commercial concept. *ACS Nano* **14**, 5183–5193 (2020).
25. Xu, Q. et al. A solution-processed zero-dimensional all-inorganic perovskite scintillator for high resolution gamma-ray spectroscopy detection. *Nanoscale* **12**, 9272–9732 (2020).
26. Zhang, Y. et al. Zero-dimensional Cs_4PbBr_6 perovskite nanocrystals. *J. Phys. Chem. Lett.* **8**, 961–965 (2017).
27. Zhang, Y. et al. Ligand-free nanocrystals of highly emissive Cs_4PbBr_6 perovskite. *J. Phys. Chem. C* **122**, 6493–6498 (2018).
28. Shin, M. et al. Understanding the origin of ultrasharp sub-bandgap luminescence from zero-dimensional inorganic perovskite Cs_4PbBr_6 . *ACS Appl. Energy Mater.* **3**, 192–199 (2020).
29. Chen, D., Wan, Z., Chen, X., Yuan, Y. & Zhong, J. Large-scale room-temperature synthesis and optical properties of perovskite-related Cs_4PbBr_6 fluorophores. *J. Mater. Chem. C* **4**, 10646–10653 (2016).
30. Thumu, U., Piotrowski, M., Owensbaird, B. & Kolenko, Y. V. Zero-dimensional cesium lead halide perovskites: phase transformations, hybrid structures, and applications. *J. Solid State Chem.* **271**, 361–377 (2019).
31. Williams, R. T., Wolszczak, W. W., Yan, X. & Carroll, D. L. Perovskite quantum-dot-in-host for detection of ionizing radiation. *ACS Nano* **14**, 5161–5169 (2020).
32. Almutlaq, J. M., Yin, J., Mohammed, O. F. & Bakr, O. M. The benefit and challenges of zero-dimensional perovskites. *J. Phys. Chem. Lett.* **9**, 4131–4138 (2018).
33. Zhou, L. et al. Intrinsic self-trapped emission in 0D lead-free $(\text{C}_4\text{H}_9\text{N})_2\text{2In}_2\text{Br}_{10}$ single crystal. *Angew. Chem.* **131**, 15581–15586 (2019).
34. Han, Q., Wu, W., Liu, W., Yang, Q. & Yang, Y. Temperature-dependent photoluminescence of CsPbX_3 nanocrystal films. *J. Lumin.* **198**, 350–356 (2018).
35. Gandini, M. et al. Efficient, fast and reabsorption-free perovskite nanocrystal-based sensitized plastic scintillators. *Nat. Nanotechnol.* **15**, 462–468 (2020).
36. Knoll, G. F. *Radiation Detection and Measurement* (Wiley, 2010).
37. Chen, Q. et al. All-inorganic perovskite nanocrystal scintillators. *Nature* **561**, 88–93 (2018).
38. Wang, L., Liu, H., Zhang, Y. & Mohammed, O. F. Photoluminescence origin of zero-dimensional Cs_4PbBr_6 perovskite. *ACS Energy Lett.* **5**, 87–99 (2020).
39. Zhu, W. et al. Low-dose real-time X-ray imaging with nontoxic double perovskite scintillators. *Light Sci. Appl.* **9**, 112 (2020).
40. Chen, L. et al. Comparative study on fluorescence decay time of doped ZnO crystals under α and β excitation. *Nucl. Instrum. Methods Phys. Res. Sect. A* **933**, 71–74 (2019).
41. Tong, F., Liu, B., Chen, H., Zhu, Z. & Gu, M. Enhanced light extraction of $\text{Bi}_3\text{Ge}_4\text{O}_{12}$ scintillator by graded-refractive index antireflection coatings. *Appl. Phys. Lett.* **103**, 071907 (2013).
42. Zhu, Z. et al. Improved light extraction efficiency of cerium-doped lutetium-yttrium oxyorthosilicate scintillator by monolayers of periodic arrays of polystyrene spheres. *Appl. Phys. Lett.* **102**, 071909 (2013).